RSC Advances

PAPER

View Article Online
View Journal | View Issue

Cite this: *RSC Adv.*, 2024, **14**, 35704

Reversible Zn and Mn deposition in NiFeMn-LDH cathodes for aqueous Zn–Mn batteries

Yuan Ge,[ab] Dong Pan,*[c] Lin Li,[ab] Jiaxin Fan[b] and Wei Liu[d]

Received 13th September 2024
Accepted 30th October 2024

DOI: 10.1039/d4ra06616b

rsc.li/rsc-advances

Introducing NiFeMn-Layered Double Hydroxide (LDH) as an innovative cathode material for Zn–Mn batteries, this study focuses on bolstering the electrochemical efficiency and stability of the system. We explored the effect of varying Zn/Mn molar ratio in the electrolyte on the battery's electrochemical performance and investigated the underlying reaction mechanism. Our results show that an electrolyte Zn/Mn molar ratio of 4 : 1 achieves a balance between capacity and stability, with an areal capacity of 0.20 mA h cm^{-2} at a current of 0.2 mA and a capacity retention rate of 53.35% after 50 cycles. The mechanism study reveals that during the initial charge–discharge cycle, NiFeMn–CO_3 LDH transforms into NiFeMn–SO_4 LDH, which then absorbs Zn^{2+}, Mn^{2+}, and SO_4^{2-} ions to form a stable composite substrate. This substrate enables the reversible deposition–dissolution of Mn ions, while Zn ions participate in the reaction continuously, with most Mn- and Zn-containing compounds depositing in an amorphous phase. Although further optimization is needed, our findings provide valuable insights for developing Zn–Mn aqueous batteries, highlighting the potential of LDHs as cathode substrates and the pivotal role of amorphous compounds in the reversible deposition–dissolution process.

1 Introduction

In energy storage, aqueous zinc ion batteries (AZIBs) have garnered considerable attention due to their high theoretical energy density, cost-efficiency, and inherent safety advantages, which stem from the non-flammable nature of zinc and its electrolytes.[1,2] The Zn–MnO_2 battery system, utilizing the abundant and cost-effective active material MnO_2, holds significant potential for developing high-energy density batteries.[3–5] Despite these advantages, the operational longevity of Zn–MnO_2 batteries has been challenged by MnO_2's dissolution, leading to a degradation of the cathode and a consequent loss of capacity.[6–9]

Recently, researchers have tried to reverse the adverse effects of MnO_2 dissolution by converting the dissolution/deposition process of MnO_2/Mn^{2+} into a part of the battery capacity.[10–13] This discovery has spurred significant research efforts to optimize substrate and electrolyte formulations and enhance the cyclability of MnO_2/Mn^{2+} redox reactions through additive incorporation.[14–19] The substrate is a crucial site for the reversible deposition reactions in batteries, significantly influencing their performance. Currently, researchers have utilized MnO_2,[20–24] Mg_xMnO_2 nanowires,[25] MnO_2/carbon,[26] MnO_2/MWCNT,[27] MnO_2/CNT,[28,29] MnO_2/carbon cloth,[30] carbon felt,[31] graphite felt,[32] 3D carbon nanotube foam skeleton,[33] and porous carbon[34] as Mn deposition substrates, achieving promising results in the Zn–MnO_2 battery system. Layered double hydroxides (LDH) such as NiCoFe-LDH, CoFe-LDH, NiFe-LDH, and NiMnFe-LDH exhibit excellent electrochemical activity and ion-adsorption capabilities,[35,36] positioning them as promising candidates for the construction of substrate materials for reversible zinc–manganese (Zn–Mn) deposition batteries The capacity of the battery system primarily stems from the intercalation of Zn into MnO_2 and the reversible reaction between MnO_2 and Mn^{2+}. The transformation between solid MnO_2 and aqueous Mn^{2+} is beneficial for enhancing capacity. However, issues such as excessive interphases during the reaction process and difficulty controlling the reactant phases persist.

Inspired by this, we attempted to construct a Zn–Mn reversible deposition battery system without MnO_2. Here, we proposed the use of NiFeMn-LDH as the cathode substrate for Zn–Mn reversible deposition batteries and conducted a detailed study of the battery's performance under electrolytes with different Zn/Mn molar ratios, exploring the electrochemical reaction mechanisms of Zn–Mn reversible deposition batteries. The battery test results indicate that when the Zn/Mn molar ratio is 4 : 1, the Zn–Mn reversible deposition battery achieves a good balance of capacity and cycling stability. At a current of 0.2 mA, the discharge areal capacity reaches 0.20 mA h cm^{-2},

[a]*School of Chemical Engineering and Technology, China University of Mining and Technology, Xuzhou 221116, People's Republic of China. E-mail: geyuan@lpssy.edu.cn*

[b]*School of Chemistry and Materials Engineering, Liupanshui Normal University, Liupanshui, Guizhou 553000, People's Republic of China*

[c]*School of Mining and Mechanical Engineering, Liupanshui Normal University, Liupanshui, Guizhou 553000, People's Republic of China. E-mail: pandong@lpssy.edu.cn*

[d]*CRRC Qingdao Sifang Rolling Stock Research Insititute Co Ltd, People's Republic of China*

with a capacity retention rate of 53.35% after 50 cycles. The electrochemical reaction mechanism study reveals that during the initial charge–discharge process, NiFeMn–CO_3 type LDH transforms into NiFeMn–SO_4 type LDH. The LDH substrate absorbs Zn, Mn, and SO_4^{2-} ions from the solution to form a more stable composite substrate. Mn ions undergo deposition–dissolution reactions on the composite substrate, while Zn ions participate in the reaction throughout the process, with Mn- and Zn-containing compounds primarily depositing in an amorphous phase.

Although the capacity and stability of the Zn–Mn aqueous battery constructed in this study still require further optimization, we have provided new insights and knowledge for Zn–Mn aqueous batteries: proposing the use of LDH as the cathode substrate to aid the Zn–Mn aqueous battery system, and discovering that the Zn–Mn reversible deposition–dissolution reaction is mainly accomplished through the deposition–dissolution of Mn- and Zn-containing amorphous compounds.

2 Experiment

2.1 Materials and synthesis

Nickel acetate ($NiC_4H_6O_4 \cdot 4H_2O$, ≥99.9%), ferric chloride ($FeCl_3 \cdot 6H_2O$, ≥99.9%), and manganese acetate ($MnC_4H_6O_4 \cdot 4H_2O$, ≥99.9%) were procured from Sigma-Aldrich. Urea ($CO(NH_2)_2$, ≥99.9%) and sodium citrate ($Na_3C_6H_5O_7 \cdot 2H_2O$, ≥99.9%) were also sourced from Sigma-Aldrich. All chemicals used in this study were not subjected to further purification processes.

Initially, a mixed solution was prepared by adding 0.5493 g of $NiC_4H_6O_4 \cdot 4H_2O$, 0.1718 g of $FeCl_3 \cdot 6H_2O$, 0.1650 g of $MnC_4H_6O_4 \cdot 4H_2O$, 0.6000 g of $CO(NH_2)_2$ (urea), and 0.0257 g of $Na_3C_6H_5O_7 \cdot 2H_2O$ into a 100 mL beaker. Subsequently, 60 mL of deionized water was added to the beaker, and the mixed solution was stirred at room temperature for one hour. The mixed solution was then transferred to a 100 mL reaction vessel and subjected to a reaction in an oven maintained at 160 °C for 24 hours. After cooling to room temperature, the product was washed with deionized water and centrifuged to separate the solid components, a process repeated three times. The resulting solid was dried in a vacuum oven at 80 °C for 10 hours. The dried NiFeMn-LDH was then ground into a fine powder for further characterization and electrochemical testing.

2.2 Materials characterization

Materials characterization of LDH was conducted using Rigaku SmartLab SE to confirm phase and crystallinity, ZEISS Sigma 300 SEM-EDS for morphology and elemental mapping, and Thermo Scientific K-Alpha XPS for surface chemistry analysis.

Utilizing X-ray Diffraction (XRD) to assess the phase and crystallinity of the samples under the following specific conditions: conducted on a Rigaku SmartLab SE with CuKα radiation at 0.15418 nm, scanning from 5° to 90° at 10° min^{-1}. The X-ray tube operated at 40 kV and 30 mA, with a high-speed scintillation detector for efficient data capture. Samples were prepared as fine powders for uniform measurement on a standard holder. Data analysis was facilitated by the instrument's software after collection at room temperature in a stable environment.

Scanning electron microscopy (SEM) and energy-dispersive X-ray spectroscopy (EDS) were conducted on a ZEISS Sigma 300 SEM-EDS system to elucidate the samples' detailed morphology and elemental composition. The Scanning Electron Microscope (SEM), featuring a Schottky field-emission electron gun, provides high-resolution imaging with a resolution of 1.00 nm at 15.0 kV and 1.60 nm at 1.0 kV. The electron optics feature a non-crossing beam path within the column, ensuring minimal distortion. The SEM's acceleration voltage is tunable from 0.02 to 30.0 kV in 10.0 V steps, accompanied by a probe current stability superior to 0.2% per hour across a range from 3.0 pA to 20.0 nA. The magnification range is extensive, spanning from 12× to an impressive 2 000 000×. The objective lens combines electromagnetic and electrostatic lenses, providing superior image quality. The detectors include an in-lens and an ETSE (Everhart–Thornley Secondary Electron) secondary electron detector, along with an EDS spectrometer for elemental analysis. The EDS analysis is performed at a working distance of 8.5 mm, which can be adjusted according to the specific requirements of the sample. The sample chamber dimensions are 365 mm × 275 mm, and the sample stage has precise movement capabilities with *X*, *Y*, and *Z* travels of 125 mm, 125 mm, and 50 mm, respectively, and a *T* tilt range from −10° to 90° with a full 360° (*R*) rotation for comprehensive sample orientation. The image acquisition system can capture high-resolution images up to 32k × 24k pixels.

X-ray photoelectron spectroscopy (XPS) was performed on a Thermo Scientific K-Alpha XPS system to investigate the samples' elemental and chemical state composition. Using an AlKα X-ray source with a photon energy ($h\nu$) of 1486.60 eV, the system was operated at a working voltage of 12.0 kV and a filament current of 6.0 mA. The analysis chamber maintained a higher vacuum level than 5.0×10^{-7} mBar to ensure a clean and contamination-free environment. The analysis utilized a focused X-ray spot size of 400 μm for precise surface analysis. For obtaining the full survey spectrum, a pass energy of 100.0 eV and a step size of 1.0 eV were utilized, whereas high-resolution narrow scans were performed with a pass energy of 50.0 eV and a step size of 0.1 eV. The system was equipped with charge neutralization to mitigate sample charging during data collection.

2.3 Electrochemical performance

The electrochemical performance of Zn–Mn batteries utilizing LDH substrates with varying Zn to Mn molar ratios was assessed *via* 2032 button cells. The LDH powder was homogeneously mixed with polyvinylidene fluoride (PVDF) as a binder and super P carbon black as a conductive agent in an 8 : 1 : 1 weight ratio to form a slurry, subsequently applied onto a graphite foil current collector. The 2032 button cells were assembled with the LDH-based electrode as the working electrode, a zinc metal foil as the counter electrode, and a glass fiber separator soaked in a mixed electrolyte containing varying Zn/Mn molar ratios of

zinc sulfate and magnesium sulfate. Galvanostatic charge–discharge tests and cyclic voltammetry (CV) were conducted using a LANDHE CT3002A electrical battery testing system and Princeton electrochemical workstation PARSTAT 4000A to assess the electrochemical performance of the LDH-based Zn–Mn battery system.

3. Results and discussion

The phase structure of the synthesized LDH was examined using X-ray diffraction (XRD) technology. As depicted in Fig. 1, diffraction peaks are observed at 11.22°, 22.64°, 33.38°, 34.22°, 38.60°, 45.87°, 59.66°, 61.11°, and 64.88° in the XRD pattern of the product. These peaks correspond to the (003), (006), (101), (012), (015), (018), (110), (113), and (116) crystal planes of $Ni_{0.75}Fe_{0.25}(CO_3)_{0.125}(OH)_2 \cdot 0.38H_2O$ (PDF-040-0215), respectively.[37,38] This indicates that the synthesized product possesses a structure analogous to that of $Ni_{0.75}Fe_{0.25}(CO_3)_{0.125}(OH)_2 \cdot 0.38H_2O$. The microstructural analysis of the synthesized LDH was conducted using Scanning Electron Microscope (SEM) and Energy Dispersion Spectrum (EDS) to elucidate the morphology and element distribution. In Fig. 2, the LDH particles exhibit a diameter of approximately 10 microns, which are constituted by numerous flake-like subunits measuring around 1 micron in size. In the Zn–Mn deposition-type battery system, the basal plane formed by stacking LDH (Layered Double Hydroxides) flake-like structures offers favourable ionic diffusion pathways and deposition sites for the reversible deposition of Zn and Mn ions. To further probe the elemental composition of the LDH, Energy Dispersion Spectrum (EDS) was employed. The EDS spectrum, as shown in Fig. 2, confirms the presence of carbon (C), manganese (Mn), iron (Fe), nickel (Ni), and oxygen (O) within the LDH structure. Concurrently, the distribution of the five elements above exhibits a strong correlation, indicating that the synthesized LDH are of the (Ni, Mn) Fe-LDH composition, with carbonate anions intercalated within the layers of the LDH structure.

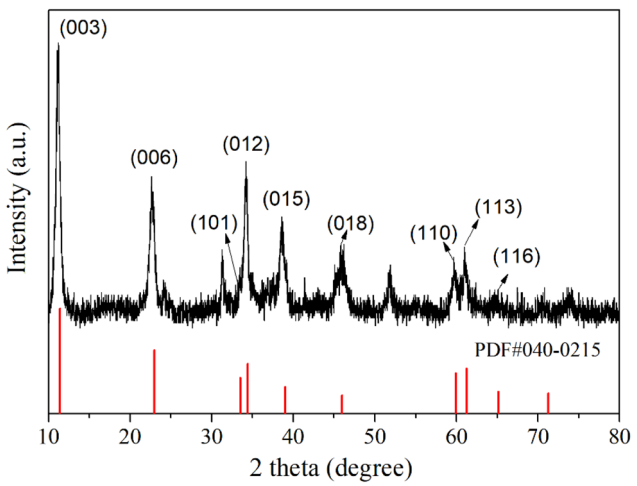

Fig. 1 XRD characterization of synthesized layered double hydroxides.

The surface chemical composition and electronic states of the synthesized LDH were investigated using X-ray photoelectron spectroscopy. The XPS high-resolution spectrum of Mn 2p, Fe 2p, Ni 2p, C 1s, and O 1s regions are depicted in Fig. 3. The Ni 2p high-resolution XPS spectrum (Fig. 3(a)) exhibits peaks from 850 to 880 eV, with the Ni $2p_{3/2}$ main peak at 855.48 eV and a satellite peak at 861.48 eV, both characteristic of Ni(II).[38–40] The Ni $2p_{1/2}$ peak at 873.18 eV and the observed spin–orbit splitting confirm the presence of divalent nickel in the sample. The Fe 2p XPS high-resolution spectrum (Fig. 3(b)) shows a main Fe $2p_{3/2}$ peak at 712.55 eV, alongside a Fe $2p_{1/2}$ peak at 725.48 eV, both characteristic of Fe(III).[38,41–43] The absence of a satellite peak suggests a minimal presence of Fe(II), indicating that the sample primarily comprises trivalent iron, which is essential for its physicochemical properties. The XPS peaks of Mn $2p_{3/2}$ (Fig. 3(c)) can be deconvoluted into three distinct peaks at 638.38 eV, 643.38 eV, and 648.75 eV, corresponding to Mn(II), Mn(III), and Mn(IV), respectively, with Mn(III) being the predominant species.[34,41,44] In the C 1s XPS high-resolution spectrum (Fig. 3(d)), three peaks are observed at 284.48 eV, 286.18 eV, and 288.46 eV, corresponding to C–C, C–O–H, and C=O (carbonate group) respectively,[45–47] which indicates that the intercalated anions in the synthesized LDH are primarily carbonates, consistent with the scanning electron microscopy-energy dispersion spectrum analysis (SEM-EDS) findings. The O 1s high-resolution XPS spectrum (Fig. 3(e)) features four peaks at binding energy of 529 to 533 eV, which can be attributed to M–O–M (M = Ni, Fe, Mn), M–O–H, O–H, and O–C within the hydroxide layers of the LDH.[39,41] The faint peak observed at a binding energy of 192.28 eV in the Cl 2p high-resolution XPS spectrum (Fig. 3(f)) suggests the presence of a minor amount of Cl^- within the layered structure of the LDH.[48] However, due to the low concentration of Cl^-, it remains undetected in the EDS analysis.

In the following, we utilize synthetically prepared layered double hydroxides (LDH) as the cathode substrate for a Zn–Mn reversible deposition battery, with zinc sheets serving as the anode and an electrolyte composed of a mixture of zinc sulfate and manganese sulfate in varying proportions. Button cells are assembled, and their charge–discharge performance is tested, as depicted in Fig. 4.

As depicted in Fig. 4(a), with a Zn to Mn molar ratio of 1 : 0 in the electrolyte, the areal capacity of the battery reaches 0.04 mA h cm^{-2}, suggesting that a Zn–Mn reversible deposition battery cannot be formed in the absence of Mn in the electrolyte, and the minimal capacity may originate from the slight intercalation of Zn into the LDH.[14,41] In Fig. 4(b), when the molar ratio of Zn to Mn in the electrolyte is 1 : 1, the first discharge areal capacity of the battery reaches 0.56 mA h cm^{-2}. Given the ionic radii of Zn^{2+} (0.074 nm) and Mn^{2+} (0.085 nm) and the minimal capacity observed in Fig. 3(a), it is apparent that the battery's capacity is predominantly attributed to the reversible deposition of Zn and Mn, rather than their reversible intercalation/deintercalation. Additionally, three distinct discharge platforms are observable on the discharge curve, at 1.53 V, 1.35 V, and 1.12 V, corresponding to the stepwise

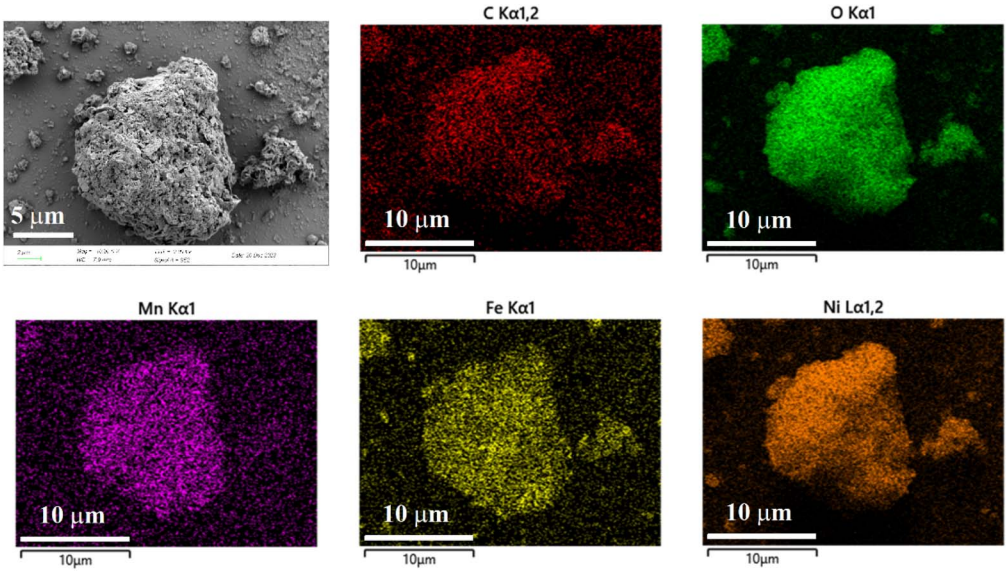

Fig. 2 SEM-EDS characterization of synthesized layered double hydroxides.

reduction of Mn^{4+} to Mn^{2+} during the dissolution process, with the charging process being the reverse deposition.[33,34,49]

Comparing the first discharge areal capacities of the batteries from Fig. 4(b)–(f) reveals that as the Zn/Mn molar ratio in the electrolyte increases, the areal capacity of the battery continually decreases. When the Zn/Mn molar ratio is 5 : 1, the first discharge areal capacity of the battery is only 0.18 mA h cm^{-2}. An interesting phenomenon is also observed: although the first discharge areal capacity reaches 0.56 mA h cm^{-2} when the Zn/Mn molar ratio is 1 : 1, the discharge areal capacity drops to 0.41 mA h cm^{-2} by the third cycle. Conversely, a Zn/Mn molar ratio of 4 : 1 in the battery can strike a balance between areal capacity and stability. Further comparisons of the rate and cycling performance of the batteries under different Zn/Mn molar ratio electrolytes will be conducted better to observe the relationship between areal capacity and stability.

In the subsequent experiments, we utilized synthetically prepared layered double hydroxides (LDH) as the cathode substrate for a Zn–Mn reversible deposition battery, with an area of 1.54 cm^2 and an LDH loading of 2 mg. Zinc sheets were employed as the anode, with an area of 2.00 cm^2 and a thickness of 0.4 mm. The electrolyte was a mixture of varying proportions of zinc sulfate and manganese sulfate. Button cells were assembled, and their rate performance and cycling stability were tested. For the rate tests, the currents were set at 0.2 mA, 0.4 mA, 0.6 mA, 0.8 mA, 1.0 mA, and 1.2 mA, with each

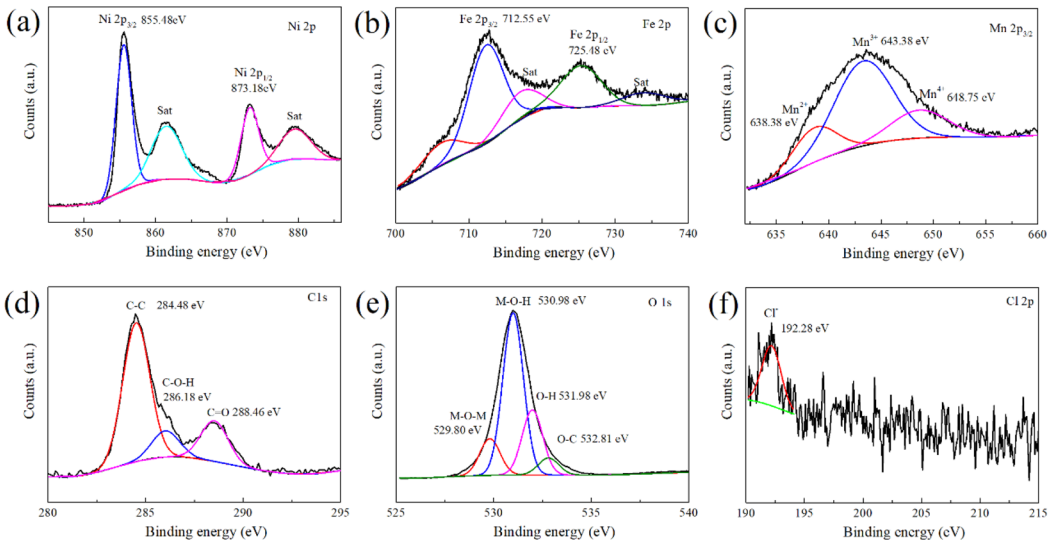

Fig. 3 XPS spectrum of the layered double hydroxides. (a) Ni 2p (b) Fe 2p (c) Mn 2p (d) C 1s (e) O 1s (f) Cl 2p.

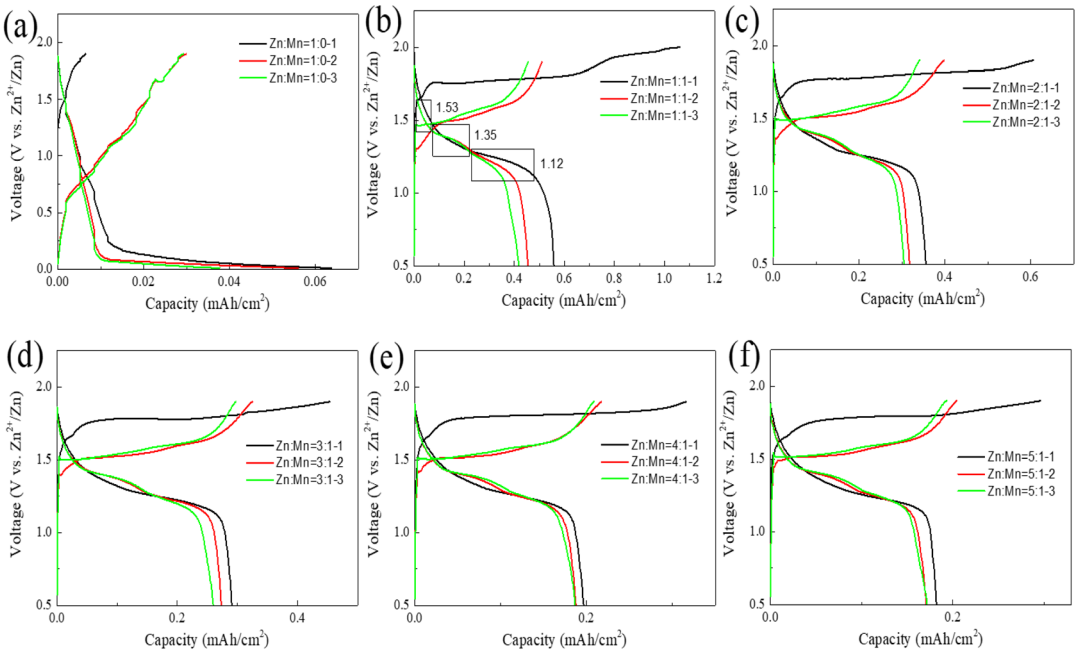

Fig. 4 Charge and discharge curves of Zn–Mn batteries based on LDHs substrate with varying Zn to Mn molar ratios in the electrolyte at a current of 0.2 mA. (a) Zn : Mn = 1 : 0 (b) Zn : Mn = 1 : 1 (c) Zn : Mn = 2 : 1 (d) Zn : Mn = 3 : 1 (e) Zn : Mn = 4 : 1 (f) Zn : Mn = 5 : 1.

condition subjected to 5 cycles. The cycling tests were conducted at a current of 0.2 mA over 50 cycles, as illustrated in Fig. 5.

In Fig. 5(a), the battery exhibits an initial discharge areal capacity of 0.04 mA h cm^{-2} at a Zn/Mn molar ratio of 1 : 0 in the electrolyte, with a charge–discharge current of 0.2 mA. The areal capacity approaches 0.01 mA h cm^{-2} during rate and cycling tests. In Fig. 5(b), at an electrolyte Zn/Mn molar ratio of 1 : 1 and a charge–discharge current of 0.2 mA, the battery's initial discharge areal capacity peaks at 0.56 mA h cm^{-2}. With an increase in the charge–discharge current to 1.2 mA, the discharge areal capacity progressively declines to 0.05 mA h cm^{-2}. Upon reducing the charge–discharge current back to 0.2 mA, the battery's discharge areal capacity partially recovers to 0.30 mA h cm^{-2}, reflecting an area capacity retention rate of 53.35%. After 50 cycles at this current, the discharge areal capacity further diminishes to 0.06 mA h cm^{-2}, with a cumulative capacity retention rate of 20.69%. The battery's coulombic efficiency exhibits notable fluctuations, suggesting that at a 1 : 1 Zn/Mn molar ratio in the electrolyte, the initial

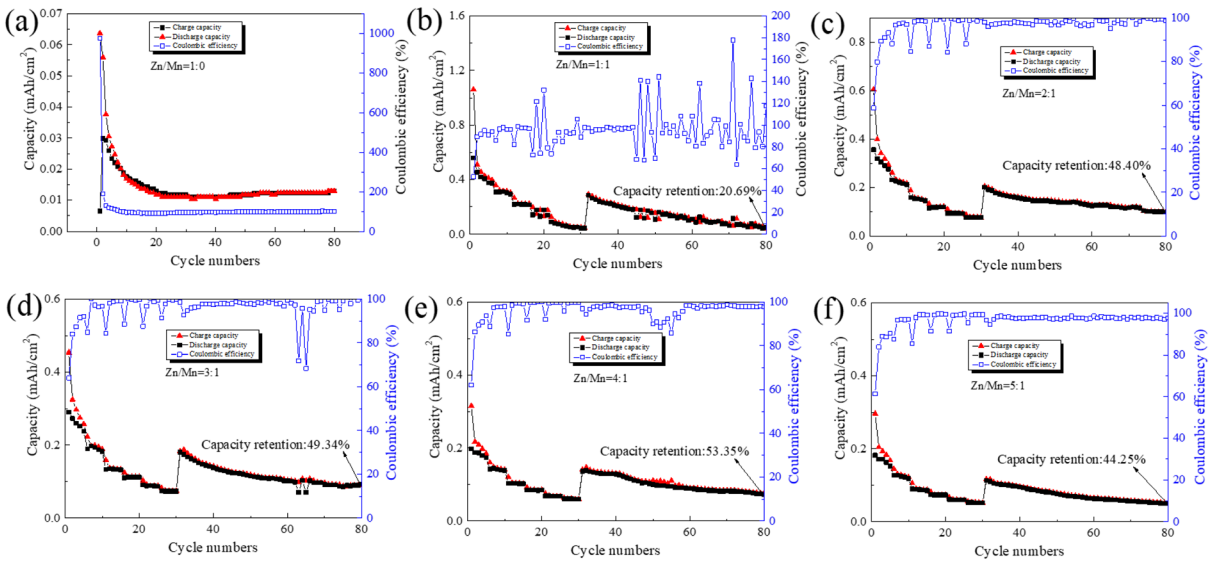

Fig. 5 Rate capability and cycling stability of Zn–Mn batteries based on LDHs substrate with varying Zn to Mn molar ratios in the electrolyte (a) Zn : Mn = 1 : 0 (b) Zn : Mn = 1 : 1 (c) Zn : Mn = 2 : 1 (d) Zn : Mn = 3 : 1 (e) Zn : Mn = 4 : 1 (f) Zn : Mn = 5 : 1.

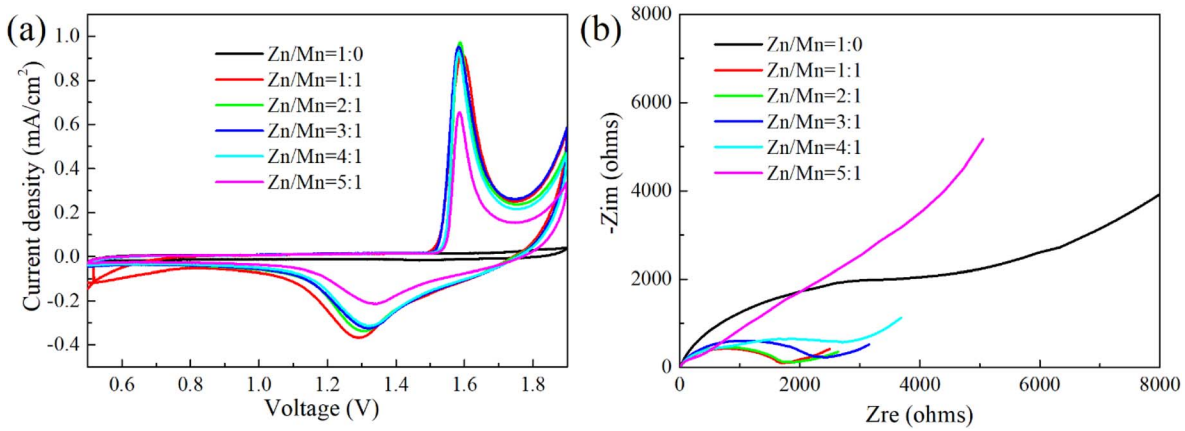

Fig. 6 (a) Cyclic voltammetry (CV) at a scan rate of 1 mV s^{-1} (b) electrochemical impedance spectroscopy (EIS) at a frequency range from 10^5 to 0.1 Hz in analysis of Zn–Mn batteries based on LDHs substrate with varying Zn to Mn molar ratios in the electrolyte.

Table 1 R_s and R_{ct} of cells with varying Zn to Mn molar ratios in the electrolyte

Zn to Mn molar ratios in the electrolyte	R_s/ohms	R_{ct}/ohms
1 : 0	5.27	4651
1 : 1	9.36	1428
2 : 1	9.94	1493
3 : 1	6.49	1798
4 : 1	4.82	2895
5 : 1	2.27	618

area capacity of the Zn–Mn reversible deposition battery is relatively high, yet the reversibility is inadequate for sustainable long-term cycling.[33,50]

Similar trends were observed in both rate and cycling tests of batteries with other Zn/Mn molar ratio electrolytes. It was also found that when the electrolyte's Zn/Mn molar ratio is 4 : 1, the initial discharge areal capacity of the battery can reach 0.20 mA h cm^{-2} in Fig. 5(e). After 30 cycles of rate testing and 50 cycles of cycling testing, the areal capacity retention rate of the battery was 53.35%, which is higher than that of batteries assembled with electrolytes of other Zn/Mn ratios. Therefore, for Zn–Mn reversible deposition batteries constructed with LDH as the cathode substrate, the Zn to Mn molar ratio in the electrolyte has a significant impact on the battery's reversibility, and a Zn/Mn molar ratio of 4 : 1 may be an appropriate electrolyte formulation.

To elucidate the electrochemical reaction mechanisms in Zn–Mn reversible deposition batteries, CV and EIS were utilized to evaluate button cells with a spectrum of Zn/Mn electrolyte ratios, with findings detailed in Fig. 6.

Fig. 6(a) shows the absence of redox peaks within the voltage range of 0.5 to 1.9 V when the electrolyte's Zn/Mn molar ratio is 1 : 0, suggesting that a Zn–Mn reversible deposition battery

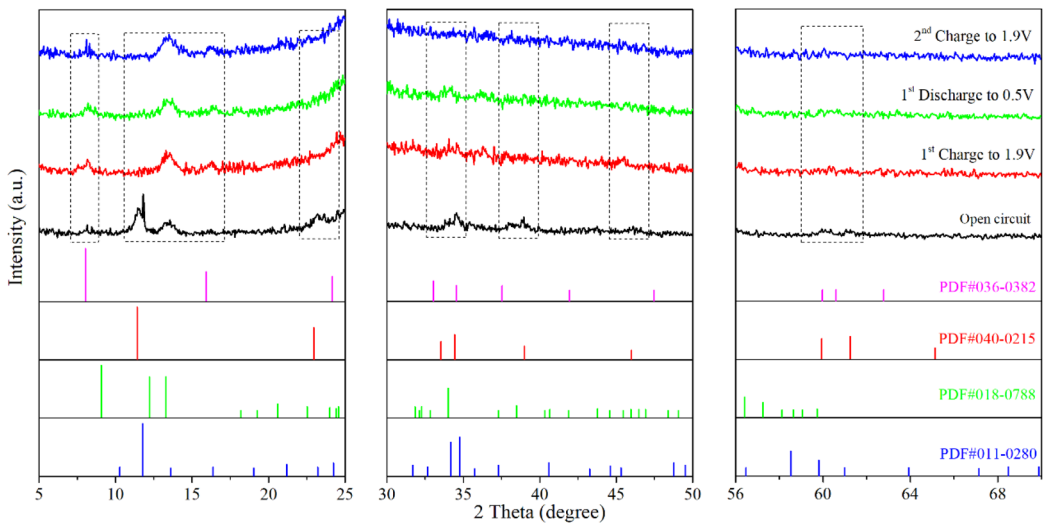

Fig. 7 *Ex situ* X-ray diffraction (XRD) analysis of Zn–Mn batteries with an LDHs substrate and a Zn/Mn molar ratio of 4 : 1 in the electrolyte under different charge–discharge states.

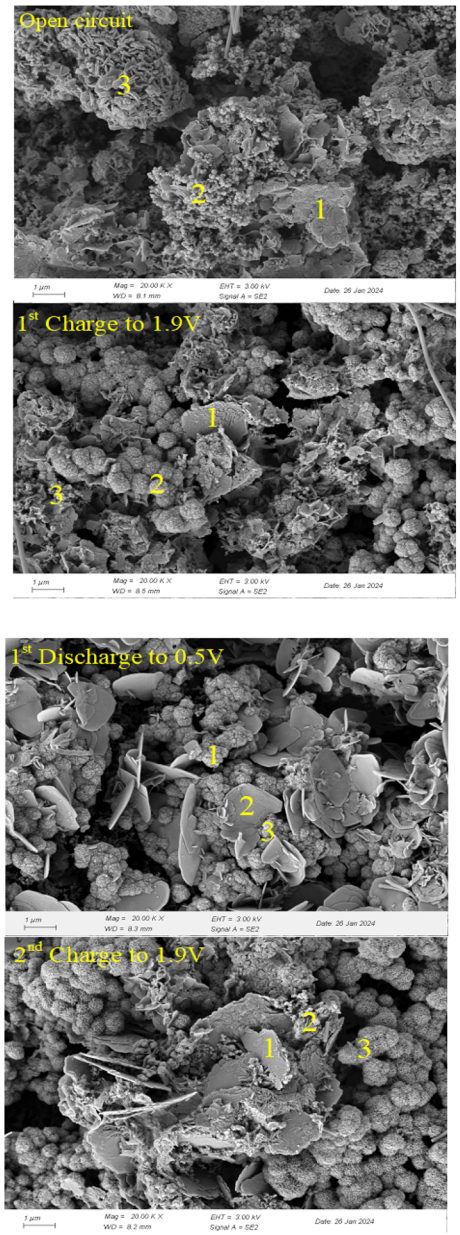

Pattern 1

Element	wt%	Wt % Sigma	At%
C	22.72	0.42	41.45
O	29.17	0.28	39.96
S	1.32	0.06	0.9
Cl	0.08	0.04	0.05
Mn	0.86	0.11	0.34
Fe	16.8	0.24	6.59
Ni	25.29	0.34	9.44
Zn	3.77	0.22	1.26
Total	100		100

Pattern 2

Element	wt%	Wt % Sigma	At%
C	36.49	0.35	54.82
O	30.84	0.26	34.78
S	0.96	0.05	0.54
Cl	0.01	0.03	0
Mn	0.79	0.09	0.26
Fe	10.13	0.18	3.27
Ni	18.53	0.27	5.69
Zn	2.24	0.16	0.62
Total	100		100

Pattern 3

Element	wt%	Wt % Sigma	At%
C	22.27	0.45	37.73
O	37.84	0.35	48.14
S	0.57	0.07	0.36
Cl	0.12	0.05	0.07
Mn	2.32	0.13	0.86
Fe	5.92	0.18	2.16
Ni	29.48	0.38	10.22
Zn	1.48	0.24	0.46
Total	100		100

Pattern 1

Element	wt%	Wt % Sigma	At%
C	15.98	0.4	31.85
O	30.43	0.26	45.54
S	2.95	0.07	2.21
Cl	0.04	0.04	0.03
Mn	12.65	0.19	5.51
Fe	6.53	0.17	2.8
Ni	13.54	0.26	5.52
Zn	17.87	0.25	6.54
Total	100		100

Pattern 2

Element	wt%	Wt % Sigma	At%
C	16.2	0.43	32.23
O	30.49	0.28	45.54
S	2.49	0.07	1.86
Cl	0.02	0.04	0.01
Mn	16.14	0.22	7.02
Fe	6.49	0.19	2.78
Ni	6.2	0.23	2.52
Zn	21.97	0.27	8.03
Total	100		100

Pattern 3

Element	wt%	Wt % Sigma	At%
C	35.86	0.35	54.2
O	30.87	0.26	35.04
S	2.23	0.06	1.26
Cl	0	0.03	0
Mn	4.11	0.12	1.36
Fe	6.01	0.15	1.95
Ni	12.01	0.24	3.71
Zn	8.92	0.18	2.48
Total	100		100

Pattern 1

Element	wt%	Wt % Sigma	At%
C	24.25	0.42	44.59
O	26.52	0.26	36.6
S	2.51	0.07	1.73
Cl	0.06	0.04	0.04
Mn	10.78	0.19	4.33
Fe	6.27	0.18	2.48
Ni	6.18	0.22	2.33
Zn	23.42	0.26	7.91
Total	100		100

Pattern 2

Element	wt%	Wt % Sigma	At%
C	15.85	0.4	34.53
O	22.87	0.22	37.4
S	3.73	0.07	3.04
Cl	0	0.04	0
Mn	12.04	0.19	5.73
Fe	9.46	0.19	4.43
Ni	9.64	0.24	4.29
Zn	26.41	0.27	10.57
Total	100		100

Pattern 3

Element	wt%	Wt % Sigma	At%
C	15.95	0.44	32.33
O	29.35	0.27	44.68
S	2.99	0.08	2.27
Cl	0.06	0.04	0.04
Mn	12.24	0.2	5.43
Fe	5.97	0.18	2.6
Ni	4.27	0.21	1.77
Zn	29.18	0.29	10.87
Total	100		100

Pattern 1

Element	wt%	Wt % Sigma	At%
C	14.47	0.42	28.39
O	34.23	0.3	50.42
S	2.47	0.07	1.81
Cl	0.1	0.04	0.07
Mn	4.7	0.14	2.02
Fe	4.94	0.15	2.08
Ni	27.3	0.33	10.96
Zn	11.8	0.26	4.25
Total	100		100

Pattern 2

Element	wt%	Wt % Sigma	At%
C	25.27	0.41	44.14
O	30.05	0.28	39.41
S	1.9	0.07	1.24
Cl	0.05	0.04	0.03
Mn	6.02	0.15	2.3
Fe	6.41	0.17	2.41
Ni	20.22	0.31	7.23
Zn	10.08	0.23	3.24
Total	100		100

Pattern 3

Element	wt%	Wt % Sigma	At%
C	14.03	0.41	30.67
O	25.13	0.24	41.24
S	2.47	0.07	2.02
Cl	0.07	0.04	0.05
Mn	23.92	0.26	11.43
Fe	7.43	0.21	3.49
Ni	5.99	0.23	2.68
Zn	20.95	0.27	8.41
Total	100		100

Fig. 8 *Ex situ* SEM morphology and elemental analysis of Zn–Mn batteries with an LDHs substrate and a Zn/Mn molar ratio of 4 : 1 in the electrolyte under different charge–discharge states.

cannot form without Mn ions,[34] corroborating the charge–discharge outcomes in Fig. 4(a). As the Zn/Mn molar ratio in the electrolyte increases from 1 : 1 to 5 : 1, distinct oxidation and reduction peaks emerge near 1.6 V and 1.3 V, respectively, in the cyclic voltammetry curves, indicating the successful construction of the Zn–Mn reversible deposition battery. Simultaneously, as the electrolyte's Zn/Mn molar ratio rises, the oxidation peak potential shifts to lower voltages while the reduction peak potential elevates, leading to a reduction in the peak potential difference. This trend suggests that a higher Zn/Mn molar ratio enhances the reversibility of the battery,[50] potentially due to the multi-element composition of the electrolyte and the facilitative effect of the LDH substrate, which will be further elucidated in the subsequent mechanistic discussion.

Based on the EIS data presented in Fig. 6(b), an equivalent circuit model for the electrode reaction was constructed and fitted to determine the solution resistance (R_s) and charge transfer resistance (R_{ct}), as detailed in Table 1.

Analysis of Table 1 reveals that at a Zn/Mn molar ratio of 1 : 0 in the electrolyte, the battery exhibited an R_s of 5.27 Ω and an R_{ct} of 4651 Ω. There was an absence of Mn redox reactions on the LDH surface, with charge transfer at the interface being significantly impeded, which is consistent with the findings depicted in Fig. 6(a). Upon increasing the Zn/Mn molar ratio to 1 : 1, the R_s decreased to 9.36 Ω and the R_{ct} to 1428 Ω, indicating

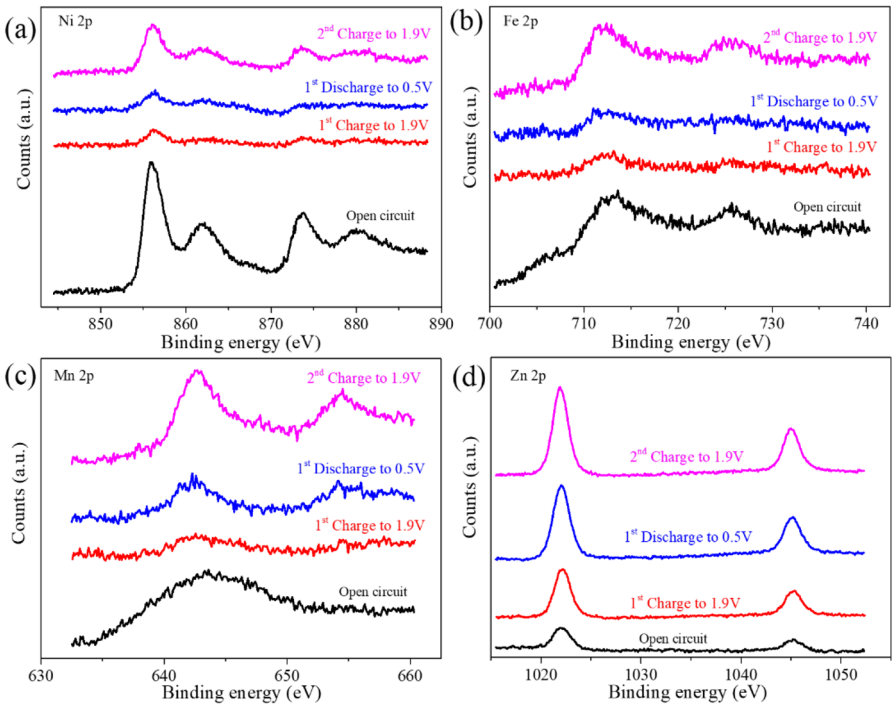

Fig. 9 *Ex situ* X-ray photoelectron spectroscopy (XPS) analysis of Zn–Mn batteries with an LDHs substrate and a Zn/Mn molar ratio of 4 : 1 in the electrolyte under different charge–discharge states. (a) Ni 2p (b) Fe 2p (c) Mn 2p (d) Zn 2p.

a marked reduction in the charge transfer impedance and the onset of Mn redox reactions at the electrode surface, corroborating the redox peaks observed in Fig. 6(a). With an increment in the Zn content within the electrolyte, the R_s and R_{ct} of the battery exhibited a trend of initial increase followed by a decrease. This behaviour is primarily attributed to the formation of zinc-containing compounds with inferior conductivity when the Zn/Mn molar ratio ranges from 1 : 1 to 4 : 1, leading to an elevation in both R_s and R_{ct}.[49] The reversible deposition of Mn on the LDH surface was obstructed, a finding supported by subsequent *ex situ* XRD and SEM-EDS analyses of the battery. At a Zn/Mn molar ratio of 5 : 1 in the electrolyte, a reduction in both R_s and R_{ct} was observed, likely due to the formation of zinc and manganese compounds with enhanced conductivity.[51] However, the competitive deposition of excess Zn directly diminished the redox activity of Mn on the LDH surface, an effect that is visually reflected in the lower capacity of mA h cm^{-2}, as illustrated in Fig. 4(f).

Fig. 7 presents the X-ray diffraction (XRD) analysis results of the cathode in the battery with a Zn/Mn molar ratio of 4 : 1 in the electrolyte under various states, including open-circuit, charged to 1.9 V, discharged to 0.5 V, and recharged to 1.9 V. In the open-circuit state, the cathode contains NiFeMn–CO_3 type (PDF No. 40-0125), NiFeMn–SO_4 type (PDF No. 36-0382)

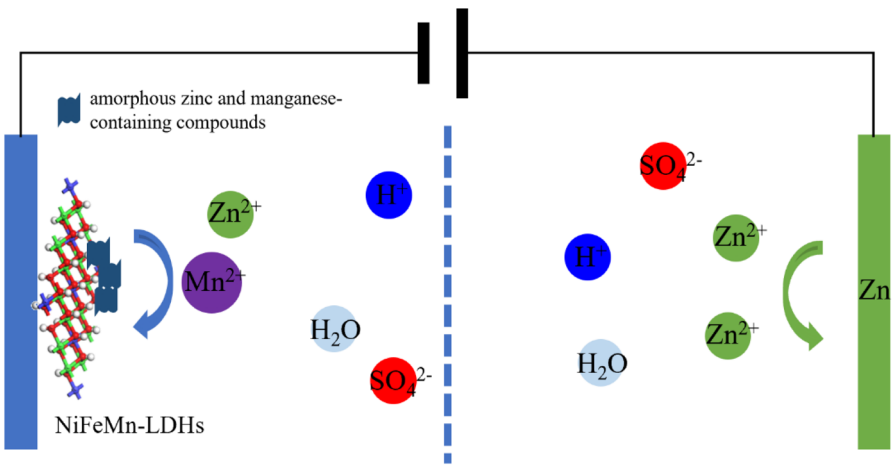

Fig. 10 The schematic illustration of the mechanism for the Zn–Mn reversible deposition battery based on LDHs.

layered double hydroxides (LDH),[52] as well as compounds containing Zn and Mn, which indicates that the experimentally synthesized NiFeMn–CO_3 type LDH, serving as the substrate for the Zn–Mn reversible deposition battery, can absorb ions such as SO_4^{2-}, Zn^{2+}, and Mn^{2+} from the electrolyte,[53,54] forming NiFeMn–SO_4 type LDH and compounds containing Zn and Mn (PDF No. 11-0280 and PDF No. 18-0788). The compounds containing Zn and Mn may exhibit a flaky structure, which will be verified through subsequent microscopic morphology observation. When the battery is charged to 1.9 V, the NiFeMn–CO_3 type LDH in the cathode disappears, while the NiFeMn–SO_4 type LDH persist, and the diffraction peaks of the compounds containing Zn and Mn become more intense and broader. Upon discharging to 0.5 V, the phase composition of the cathode is like that when charged to 1.9 V. When the battery is recharged to 1.9 V, the phase composition of the cathode is comparable to that after discharging to 0.5 V. These results suggest that in the constructed Zn–Mn reversible deposition battery system, the NiFeMn–CO_3 type LDH as the substrate absorbs SO_4^{2-}, Zn^{2+}, and Mn^{2+} ions from the electrolyte to form more stable NiFeMn–SO_4 type LDH and compounds containing Zn and Mn. These substances collectively form the substrate and stably exist throughout the subsequent charge–discharge processes, with Zn and Mn ions undergoing reversible deposition in an amorphous structure on the new composite substrate.

To elucidate the reaction mechanisms of Zn–Mn reversible deposition batteries, SEM-EDS analysis was applied to the cathode with a Zn/Mn molar ratio of 4 : 1 in the electrolyte under different operational states, including open-circuit, charged to 1.9 V, discharged to 0.5 V, and recharged to 1.9 V, as depicted in Fig. 8. At the open-circuit state, a flaky structure was observed on the cathode, and EDS elemental analysis revealed the presence of Zn, Mn, S, and O, suggesting the possible formation of zinc and manganese alkaline sulfates.[33,49] Upon charging to 1.9 V, new spherical structures emerged on the cathode. Comparing the EDS elemental analysis before and after charging, a significant increase in Zn and Mn content was observed, indicating that the deposition of Zn and Mn on the cathode surface during charging is the primary source of the battery's charging capacity.[14,34] Additionally, a noticeable decrease in Ni and Fe content was detected, suggesting that the dissolution of Ni and Fe accompanies the transformation from NiFeMn–CO_3 type LDH to NiFeMn–SO_4 type LDH.

When the battery was discharged to 0.5 V, several spherical structures remained on the cathode, indicating that the newly formed composite substrate was relatively stable. Moreover, a pronounced flaky structure appeared, with corresponding EDS elemental analysis showing a significant increase in S and Zn, suggesting an increase in zinc alkaline sulfates.[33] However, a specific decrease in Mn content indicated that the manganese alkaline sulfates formed during the charging process undergo dissolution reactions. The extent of deposition and dissolution is evidently not equivalent, which may cause the battery's capacity to fade.[14,55] Upon recharging to 1.9 V, the prominent flaky structure still existed, but with noticeable irregularities at the edges, indicating that the dissolution of zinc alkaline sulfates occurs, and the released Zn ions participate in the redeposition reactions with Mn ions. Compared to the state after discharging to 0.5 V, the spherical structures were more abundant upon recharging to 1.9 V, and the Mn content increased again, indicating that the deposition reactions of Zn and Mn are primarily concentrated on the spherical structures, which are the previously mentioned composite substrates.

In summary, using NiFeMn–CO_3 type LDH as the cathode substrate in Zn–Mn reversible deposition batteries, a composite substrate containing NiFeMn–SO_4 type LDH and compounds of Zn and Mn is formed on the cathode during the open-circuit and initial charging processes. In the subsequent charge–discharge processes, reversible deposition reactions of Zn and Mn occur on the composite substrate, primarily involving the deposition and dissolution of amorphous zinc and manganese alkaline sulfates; the rates of deposition and dissolution reactions for compounds containing Zn and Mn are not consistent.

Further insight into the reaction mechanisms of Zn–Mn reversible deposition batteries is garnered through the analysis of elemental property changes on the cathode surface at a Zn/Mn molar ratio of 4 : 1 in the electrolyte during states of open-circuit, charging to 1.9 V, discharging to 0.5 V, and recharging to 1.9 V, as illustrated in Fig. 8.

Fig. 9(a) and (b) demonstrate that the binding energies of Ni $2p_{3/2}$, Ni $2p_{1/2}$, Fe $2p_{3/2}$, and Fe $2p_{1/2}$ peaks remain relatively stable throughout the battery's charge–discharge cycle. Nonetheless, a significant reduction in the corresponding peak intensities is observed during the initial charge–discharge phase. Upon recharging to 1.9 V, partial recovery of peak intensities is observed, suggesting a dissolution and reformation process from NiFeMn–CO_3 to NiFeMn–SO_4 type LDH during the initial charge–discharge cycle, which results in the formation of a novel composite substrate. This finding is consistent with the SEM-EDS analysis presented in Fig. 7. Fig. 9(c) shows that in the open-circuit state, Mn primarily exists in the divalent form within the cathode. During the initial charge–discharge cycle followed by recharging, Mn undergoes deposition and dissolution reactions. The deposition process mainly involves the oxidation of divalent Mn to tetravalent Mn, while the dissolution reaction represents the reduction of Mn. Additionally, the broadened peaks at the binding energies of 654.4 eV for Mn $2p_{1/2}$ and 642.6 eV for Mn $2p_{3/2}$ indicate the formation of compounds containing divalent, trivalent, and tetravalent Mn during the oxidation process.[34,41] Fig. 9(d) confirms the presence of Zn in the cathode during the open-circuit state, consistent with prior SEM-EDS analysis. Zn's continued presence throughout the initial charge–discharge and subsequent recharging cycles indicates its active role in the Mn deposition and dissolution processes on the cathode. The use of a selectively permeable separator is proposed to regulate Zn's influence on cathode reactions.

Finally, integrating the results from the charge–discharge performance, cycling stability, and electrochemical impedance spectroscopy of the battery, along with the *ex situ* XRD, SEM-EDS, and XPS analyses of the cathode, we propose a schematic illustration of the Zn/Mn reversible deposition battery with NiFeMn-LDH as the cathode substrate, as shown in Fig. 10. When the Zn/Mn molar ratio in the mixed electrolyte is 4 : 1, the

NiFeMn-LDH as the cathode substrate can induce Zn^{2+}, Mn^{2+}, and SO_4^{2-} ions from the electrolyte to undergo reversible dissolution–deposition reactions on its surface in the form of an amorphous mixture. At this ratio, the battery's capacity and cycling stability are well-balanced. This work provides significant insights for the construction of MnO_2-free Zn/Mn reversible deposition batteries.

3 Conclusions

In this research, we developed a reversible dissolution–precipitation aqueous battery using NiFeMn-LDH as the cathode material substrate. Through comprehensive electrochemical and microstructural characterization, we explored the battery's performance and the underlying reaction mechanisms. Results indicate that at a Zn/Mn molar ratio of 4 : 1 in the electrolyte, the battery maintains a balance between capacity and stability, achieving an area capacity of 0.2 mA h cm^{-2}. The battery's capacity is primarily attributed to the reversible dissolution–precipitation of amorphous zinc and manganese-containing compounds, enabled by the NiFeMn-LDH substrate, which offers numerous active sites for this process. Future work will focus on electrolyte optimization to enhance the reversibility of these reactions and improve the battery's cyclic stability.

Data availability

The data supporting the findings of this study are available within the article.

Author contributions

The manuscript was written through the contributions of all authors. All authors have approved the final version of the manuscript.

Conflicts of interest

There are no conflicts to declare.

Acknowledgements

The authors express their sincere gratitude for the financial support provided by The Science and Technology Plan Project of Guizhou Province [No. Qian Ke He Jichu-[2024]QingNian 016], The Scientific Research and Cultivation Project of Liupanshui Normal University (LPSSY2023KJYBPY08, LPSSY2023KJYBPY03), The Science and Technology Development Project of Liupanshui (52020-2023-0-2-7, 52020-2023-0-2-12), Liupanshui Normal University High-Level Talents Research Initiation Special Project [LPSSYKYJJ202404], Carbon Neutral Engineering Research Center of Guizhou Colleges and Universities in Coal Industry (Qian Jiao Ji[2023]No.044).

Notes and references

1 J. Li, Y. Wang, Y. Wang, Y. Guo, S. Zhang, H. Song, X. Li, Q. Gao, W. Shang, S. Hu, H. Zheng and X. Li, *Nano Mater. Sci.*, 2023, **5**, 237–245.
2 Y. Zhang, A. Chen and J. Sun, *J. Energy Chem.*, 2020, **54**, 655–667.
3 H. Zhang, Z. Shen, D. Jia, W. Zhou, X. Wang, J. Liu and X. He, *J. Alloys Compd.*, 2024, **991**, 174413.
4 Y. Zhang, S. Luo, G. Yang, L. Yu, S. Ye, C. Jiang and Y. Wu, *Mater. Lett.*, 2024, **361**, 135993.
5 Y. Ren, H. Li, Y. Rao, H. Zhou and S. Guo, *Energy Environ. Sci.*, 2024, **17**, 425–441.
6 X. Li, Z. Xu, Y. Qian and Z. Hou, *Energy Storage Mater.*, 2022, **53**, 72–78.
7 N. Zhang, Y.-R. Ji, J.-C. Wang, P.-F. Wang, Y.-R. Zhu and T.-F. Yi, *J. Energy Chem.*, 2023, **82**, 423–463.
8 Y. Wu, B. Yan, Y. Liu, J. Kong, X. Lin, M. Gong, L. Zhang and D. Wang, *J. Power Sources*, 2024, **602**, 234313.
9 H. Yao, W. Dong, X. Ji and S. Cheng, *Surf. Interfaces*, 2024, **44**, 103669.
10 T.-H. Wu, S.-L. Cheng and S.-C. Liao, *Electrochim. Acta*, 2024, **490**, 144290.
11 S. Cui, D. Zhang and Y. Gan, *J. Power Sources*, 2023, **579**, 233293.
12 H. Li, H. Yao, X. Sun, C. Sheng, W. Zhao, J. Wu, S. Chu, Z. Liu, S. Guo and H. Zhou, *Chem. Eng. J.*, 2022, **446**, 137205.
13 Y. Zhao, X. Xia, Q. Li, Y. Wang, Y. Fan, Y. Zhao, W. Liu and X. Sun, *Energy Storage Mater.*, 2024, **67**, 103268.
14 Z. Zhong, J. Li, L. Li, X. Xi, Z. Luo, G. Fang, S. Liang and X. Wang, *Energy Storage Mater.*, 2022, **46**, 165–174.
15 W. Liu, X. Zhang, Y. Huang, B. Jiang, Z. Chang, C. Xu and F. Kang, *J. Energy Chem.*, 2021, **56**, 365–373.
16 H. Wang, T. Wang, G. Stevenson, M. Chamoun and R. W. Lindström, *Energy Storage Mater.*, 2023, **63**, 103008.
17 C. Xie, T. Li, C. Deng, Y. Song, H. Zhang and X. Li, *Energy Environ. Sci.*, 2020, **13**, 135–143.
18 M. Zhang, H. Hua, P. Dai, Z. He, L. Han, P. Tang, J. Yang, P. Lin, Y. Zhang, D. Zhan, J. Chen, Y. Qiao, C. C. Li, J. Zhao and Y. Yang, *Adv. Mater.*, 2023, **35**, 2208630.
19 D. Wu, L. Housel, S. J. Kim, N. Sadique, C. Quilty, L. Wu, R. Tappero, S. Nicholas, S. Ehrlish, Y. Zhu, A. Marschilok, E. Takeuchi, D. Bock and K. Takeuchi, *Energy Environ. Sci.*, 2020, **13**, 4322–4333.
20 Z. Liu, H.-B. He, Z.-X. Luo, X.-F. Wang and J. Zeng, *Trans. Nonferrous Met. Soc. China*, 2023, **33**, 1193–1204.
21 X. Xie, H. Fu, Y. Fang, B. Lu, J. Zhou and S. Liang, *Adv. Energy Mater.*, 2022, **12**, 2102393.
22 H. Chen, C. Dai, F. Xiao, Q. Yang, S. Cai, M. Xu, H. Fan and S.-J. Bao, *Adv. Mater.*, 2022, **34**, 2109092.
23 K. Ma, Q. Li, C. Hong, G. Yang and C. Wang, *ACS Appl. Mater. Interfaces*, 2021, **13**, 55208–55217.
24 X. Xue, Z. Liu, S. Eisenberg, Q. Ren, D. Lin, E. Coester, H. Zhang, J. Z. Zhang, X. Wang and Y. Li, *ACS Energy Lett.*, 2023, **8**, 4658–4665.

25 Z. Yang, X. Pan, Y. Shen, R. Chen, T. Li, L. Xu and L. Mai, *Small*, 2022, **18**, 2107743.
26 V. R. Kankanallu, X. Zheng, D. Leschev, N. Zmich, C. Clark, C.-H. Lin, H. Zhong, S. Ghose, A. M. Kiss, D. Nykypanchuk, E. Stavitski, E. S. Takeuchi, A. C. Marschilok, K. J. Takeuchi, J. Bai, M. Ge and Y.-C. K. Chen-Wiegart, *Energy Environ. Sci.*, 2023, **16**, 2464–2482.
27 D. Wu, S. T. King, N. Sadique, L. Ma, S. N. Ehrlich, S. Ghose, J. Bai, H. Zhong, S. Yan, D. C. Bock, E. S. Takeuchi, A. C. Marschilok, L. M. Housel, L. Wang and K. J. Takeuchi, *J. Mater. Chem. A*, 2023, **11**, 16279–16292.
28 Z. R. Mansley, Y. Zhu, D. Wu, E. S. Takeuchi, A. C. Marschilok, L. Wang and K. J. Takeuchi, *Nano Lett.*, 2023, **23**, 8657–8663.
29 D. Wu, L. M. Housel, S. T. King, Z. R. Mansley, N. Sadique, Y. Zhu, L. Ma, S. N. Ehrlich, H. Zhong, E. S. Takeuchi, A. C. Marschilok, D. C. Bock, L. Wang and K. J. Takeuchi, *J. Am. Chem. Soc.*, 2022, **144**, 23405–23420.
30 P. Ruan, X. Xu, D. Zheng, X. Chen, X. Yin, S. Liang, X. Wu, W. Shi, X. Cao and J. Zhou, *ChemSusChem*, 2022, **15**, e202201118.
31 C. Tamtong, W. Kao-ian, P. Kidkhunthod and S. Kheawhom, *Integr. Ferroelectr.*, 2023, **238**, 216–223.
32 C. Yan, X. Tong, Y. Qu, Y. Zhou, N. Pang, S. Xu, D. Xiong, L. Wang and P. K. Chu, *Vacuum*, 2021, **191**, 110353.
33 X. Shen, X. Wang, Y. Zhou, Y. Shi, L. Zhao, H. Jin, J. Di and Q. Li, *Adv. Funct. Mater.*, 2021, **31**, 2101579.
34 H. Moon, K.-H. Ha, Y. Park, J. Lee, M.-S. Kwon, J. Lim, M.-H. Lee, D.-H. Kim, J. H. Choi, J.-H. Choi and K. T. Lee, *Adv. Sci.*, 2021, **8**, 2003714.
35 D. Qiu, H. Wang, T. Ma, J. Huang, Z. Meng, D. Fan, C. R. Bowen, H. Lu, Y. Liu and S. Chandrasekaran, *ACS Nano*, 2024, **18**, 21651–21684.
36 F. Ran, M. Hu, S. Deng, K. Wang, W. Sun, H. Peng and J. Liu, *RSC Adv.*, 2024, **14**, 11482–11512.
37 Y. Zhao, P. Zhang, J. Liang, X. Xia, L. Ren, L. Song, W. Liu and X. Sun, *Adv. Mater.*, 2022, **34**, 2204320.
38 Q. Ding, J. Li, S. Li, J. Wang, W. Huang, S. Sun, Y. Xu and H. Li, *J. Energy Storage*, 2023, **67**, 107556.
39 J. Meng, Y. Song, Z. Qin, Z. Wang, X. Mu, J. Wang and X.-X. Liu, *Adv. Funct. Mater.*, 2022, **32**, 2204026.
40 M. Rastgoo-Deylami and A. Esfandiar, *ACS Appl. Energy Mater.*, 2021, **4**, 2377–2387.
41 Y. Zhao, P. Zhang, J. Liang, X. Xia, L. Ren, L. Song, W. Liu and X. Sun, *Adv. Mater.*, 2022, **34**, 2204320.
42 X. Xuan, M. Qian, L. Pan, T. Lu, Y. Gao, L. Han, L. Wan, Y. Niu and S. Gong, *J. Energy Chem.*, 2022, **70**, 593–603.
43 S. Chandrasekaran, R. Hu, L. Yao, L. Sui, Y. Liu, A. Abdelkader, Y. Li, X. Ren and L. Deng, *Nano-Micro Lett.*, 2023, **15**, 48.
44 C. Wang, C. Zhou, B. Zhang, X. Ou, L. Cao, C. Peng and J. Zhang, *RSC Adv.*, 2019, **9**, 9075–9078.
45 L. Chai, A. Bala Musa, J. Pan, J. Song, Y. Sun and X. Liu, *J. Power Sources*, 2022, **544**, 231887.
46 H.-M. Kim, B.-C. Cha and D.-W. Kim, *RSC Adv.*, 2023, **13**, 26918–26924.
47 C. Xu, L. Zhang, F. Liu, R. Zhang and H. Yue, *RSC Adv.*, 2024, **14**, 12454–12462.
48 Z. Wu, Y. Wu, Q. Yuan, J. Zhang, Y. Dou and J. Han, *ACS Appl. Mater. Interfaces*, 2023, **15**, 38540–38549.
49 X. Guo, J. Zhou, C. Bai, X. Li, G. Fang and S. Liang, *Mater. Today Energy*, 2020, **16**, 100396.
50 X. Yang, Z. Jia, W. Wu, H.-Y. Shi, Z. Lin, C. Li, X.-X. Liu and X. Sun, *Chem. Commun.*, 2022, **58**, 4845–4848.
51 X. Yang, Z. Jia, W. Wu, H.-Y. Shi, Z. Lin, C. Li, X.-X. Liu and X. Sun, *Chem. Commun.*, 2022, **58**, 4845–4848.
52 H. Yi, S. Liu, C. Lai, G. Zeng, M. Li, X. Liu, B. Li, X. Huo, L. Qin, L. Li, M. Zhang, Y. Fu, Z. An and L. Chen, *Adv. Energy Mater.*, 2021, **11**, 2002863.
53 Y. Wang, Q. Pan, Y. Qiao, X. Wang, D. Deng, F. Zheng, B. Chen and J. Qiu, *Adv. Mater.*, 2023, **35**, 2210871.
54 L. Zhang, T. Zhang, Y. Zhao, G. Dong, S. Lv, S. Ma, S. Song and M. Quintana, *Nano Res.*, 2023, **17**, 1646–1654.
55 L. Wei and Z. Gao, *RSC Adv.*, 2023, **13**, 8427–8463.